Rainbow scattering under axial surface channeling from a KCl(001) surface

U. Specht, M. Busch,* J. Seifert, A. Schüller, and H. Winter
Institut für Physik, Humboldt-Universität zu Berlin, Newtonstrasse 15, D-12489 Berlin-Adlershof, Germany

K. Gärtner
Institut für Festkörperphysik, Friedrich-Schiller-Universität Jena, Max-Wien-Platz 1, D-07743 Jena, Germany

R. Włodarczyk, M. Sierka, and J. Sauer
Institut für Chemie, Humboldt-Universität zu Berlin, Brook-Taylor-Strasse 2, D-12489 Berlin-Adlershof, Germany
(Received 23 May 2011; revised manuscript received 14 July 2011; published 28 September 2011)

Fast He, Ne, Ar, and N atoms with projectile energies from 1 up to 60 keV are scattered under grazing polar angles of incidence from a flat and clean KCl(001) surface. For the scattering along low-index directions (axial surface channeling) we observe pronounced peaks in the angular distributions of scattered projectiles which can be attributed to rainbow scattering. From classical trajectory calculations based on universal and individual pair as well as density functional theory (DFT) potentials, we obtained corresponding rainbow angles for comparison with the experimental data. Fair agreement was found for DFT and individual pair potentials calculated from Hartree-Fock wave functions.

DOI: 10.1103/PhysRevB.84.125440 PACS number(s): 68.49.Bc, 34.20.Cf, 34.35.+a, 34.50.−s

I. INTRODUCTION

For the description of atomic collisions the interaction potentials are essential to determine the trajectories of the collision partners and the differential cross sections.[1,2] Accordingly, stopping phenomena, electronic excitation, charge transfer processes, sputtering, etc., are directly related to the interatomic potentials between the collision partners.[3] Examples for the importance of the interatomic potentials are low- and medium-energy ion scattering spectroscopy (LEIS[4,5] and MEIS,[6,7] respectively), where the potential determines the shape of the shadow and blocking cone.[4] In collisions of fast atoms and ions with insulator surfaces under grazing angles of incidence with respect to the surface plane, one can observe interesting phenomena as high electron yields, large fractions of negative ions, suppression of charge transfer, and resonant coherent excitation of projectiles. For the interpretation of such features and modeling of the microscopic interaction mechanism, accurate interaction potentials are important.

In the regime of surface channeling, the scattering potential results from an averaging over discrete interatomic potentials between a projectile atom or ion and the atoms of the target surface. This leads to an effective potential with either *planar* symmetry when the projectiles are steered by planes (*planar surface channeling*) or axial symmetry for steering along axial strings (low-index directions) of surface atoms (*axial surface channeling*).[8] An important feature resulting from such an averaged potential is the distance of closest approach of projectiles to the surface plane, which is essential for the theoretical description of interaction processes of atoms or ions in front of a surface. Along the low-index directions of the surface plane the interaction potential is quasisinusoidally corrugated. This corrugation gives rise to extrema of the deflection function $\theta(b)$, which is the dependence of the scattering angle θ on the impact parameter b, leading to an enhanced flux of scattered projectiles under a maximum deflection angle, the so-called *rainbow angle* θ_{rb} in analogy to the atmospheric phenomenon. Rainbow scattering is a fairly general phenomenon in atom-atom and atom-surface collisions. For a general discussion on this topic we refer to the literature (see, e.g., Refs. 9–12 and the review by Kleyn and Horn[13]).

Recently, we have demonstrated that detailed information on the effective interaction potential at metal and insulator surfaces can be derived from rainbow structures.[14–21] These structures can be observed in the angular distributions after scattering of fast atoms along low-index directions of the surface plane of monocrystalline samples and can be compared with results from classical trajectory calculations. We have shown that the rainbow angle θ_{rb} is sensitive and therefore suitable for probing the interaction potential in the classical regime, where quantum-mechanical effects can be neglected and the quasistatic limit applies.

In this work we present a study on the scattering of fast He, Ne, Ar, and N atoms from a KCl(001) surface along ⟨100⟩ and ⟨110⟩ directions under grazing angles of incidence with respect to the surface plane. The experimental results are compared with classical trajectory calculations based on three different types of potentials: (i) the universal Ziegler-Biersack-Littmark (ZBL[3]) and O'Connor-Biersack (OCB[22]) potentials, (ii) individual pair potentials calculated from Hartree-Fock wave functions, and (iii) density functional theory (DFT) potentials. The individual Hartree-Fock (HF) pair potentials calculated within the present work were compared with the HF potentials calculated by Kim and Gordon[23,24] as well as with the universal potentials.

II. EXPERIMENT

The experiments were performed in an ultrahigh vacuum chamber at a base pressure in the 10^{-11} mbar range, attached via two differential pumping stages to the beam line of an electrostatic ion accelerator. In the experiments, we have scattered neutral He, Ne, Ar, and N atoms with projectile energies E_0 ranging from 1 keV up to 60 keV from a flat and

clean KCl(001) surface at room temperature under grazing polar angles of incidence ϕ_{in} ranging from 0.5° up to 2° with respect to the surface plane. These settings provide normal energies (kinetic energy for motion along the surface normal) $E_\perp = E_0 \sin^2 \phi_{in}$ ranging from 0.5 eV up to 40 eV. The azimuthal setting of the target surface was oriented along the ⟨100⟩ or ⟨110⟩ low-index directions in the surface plane. The fast ion beams were produced in a 10-GHz electron cyclotron resonance (ECR) ion source (Nanogan-Pantechnique, Caen, France). The neutralization of ions was achieved via charge transfer in a gas cell mounted in the beam line of the accelerator operating with He, Ne, Ar, or N_2 gas. Residual ions were removed by electric field plates. The atomic beams were collimated by two sets of vertical and horizontal slits of 0.2-mm widths to a beam divergence smaller than 0.03° (adjustable).

The KCl(001) surface was prepared by cycles of grazing sputtering with 25-keV Ar^+ ions at a temperature of 470 K and subsequent annealing at about 650 K for 20 min. Two-dimensional angular distributions of scattered projectiles were recorded at a distance of 0.66 m behind the target with a position-sensitive microchannel plate (MCP) detector (Roentdek GmbH, Kelkheim-Ruppertshain, Germany). In order to avoid dead-time effects in the data acquisition system, the count rate was reduced to less than 10^4 counts per second. At such a low flux of particles in the range of sub-fA, radiation damage of the target surface via sputtering or implantation effects can be completely neglected. The charge state of incoming and scattered projectiles was checked by means of electric field plates between target and detector. In general, the fraction of ions in the scattered beam was found to be negligibly small.

III. RESULTS AND DISCUSSION

A. Calculation of channeling potentials

For axial surface channeling, the averaged interaction potential between a projectile and the target surface is given by

$$V_{surface}(x,z) = \sum_{-\infty}^{+\infty} V_{string,n}(\sqrt{(x-x_n)^2 + (z-z_n)^2}), \quad (1)$$

where $V_{string,n}$ is the interaction potential between the projectile and a string of atoms at positions (x_n, z_n) averaged over the low-index surface channeling direction (y direction). The direction within the surface plane transverse to the channeling direction defines the x coordinate, and z is the coordinate normal to the surface plane. The summation runs over all atomic strings forming the surface. For one-atomic strings the corresponding potential is given by[25–28]

$$V_{string}(\xi) = \frac{1}{d}\int_{y_0}^{y_0+d} V(\sqrt{\xi^2 + y^2})dy, \quad (2)$$

where d is the distance between adjacent atoms within the string and $V(\sqrt{\xi^2 + y^2}) = V(r)$ is the interaction potential between the projectile and a string atom as function of their distance $r = \sqrt{\xi^2 + y^2}$, with $\xi = \sqrt{x^2 + z^2}$. We note that this averaging results immediately from the fast parallel motion of the projectile (with the kinetic energy $E_{||} = E_0 \cos^2 \phi_{in} \approx E_0$, which is approximately the projectile energy E_0 in the regime of grazing scattering) above the surface, and therefore, we considered this averaging in the classical trajectory calculations. For the ⟨110⟩ direction within the (001) surface of KCl there are two different kinds of one-atomic strings, consisting of K and Cl atoms or ions only, providing two different string potentials. However, in the case of the ⟨100⟩ direction there exists only one kind of string consisting of alternating K and Cl atoms or ions. The corresponding string potential reads

$$V_{string}(\xi) = \tfrac{1}{2}[V_{string,K}(\xi) + V_{string,Cl}(\xi)]. \quad (3)$$

If the interaction potential $V(r)$ between two atoms (e.g., a projectile and a target atom of the surface) with nuclear charge numbers Z_1 and Z_2 and the distance r can be described as screened Coulomb potential (all energies and lengths in atomic units, a.u.),

$$V(r) = \frac{Z_1 Z_2}{r}\Phi(r) = \frac{Z_1 Z_2}{r}\sum_{i=1}^{N} a_i \exp(-b_i r/a_s), \quad (4)$$

with a screening function $\Phi(r)$, which can be written as a sum of exponential functions with a screening length a_s, the integral in Eq. (2) can be calculated analytically:[8,27–30]

$$V_{string}(\xi) = \frac{2Z_1 Z_2}{d}\sum_{i=1}^{N} a_i K_0(b_i \xi/a_s), \quad (5)$$

with K_0 being the modified zeroth-order Bessel function of the second kind (Macdonald function[31]). Hence, the averaged force $\vec{F}_{string}(\vec{\xi}) = -\vec{\nabla} V_{string}(\xi)$ between the projectile and an atomic string is given by

$$\vec{F}_{string}(\vec{\xi}) = \frac{2Z_1 Z_2}{d}\sum_{i=1}^{N} a_i b_i K_1(b_i \xi/a_s)\frac{\vec{\xi}}{\xi}, \quad (6)$$

where $-\partial K_0(\xi)/\partial\xi = K_1(\xi)$ is the modified first-order Bessel function of the second kind. The resulting force $\vec{F}_{surface}(x,z)$ between the projectile and the target surface is given by the sum of the atomic string forces $\vec{F}_{string}(\vec{\xi})$ analogously to Eq. (1). The analytical expression of $\vec{F}_{surface}(x,z)$ is used for the classical trajectory calculations, where the trajectories of the scattered projectiles are derived from Newton's law for the two-dimensional motion in the xz plane by solving the initial value problem using the Runge-Kutta method.

The screening function of the universal ZBL potential[3] is given by a sum of four exponential functions with the parameters $a_i = \{0.1818, 0.5099, 0.2802, 0.02817\}$ and $b_i = \{3.2, 0.9423, 0.4028, 0.2016\}$ with the ZBL screening length $a_s = a_{ZBL} = 0.8854/(Z_1^{0.23} + Z_2^{0.23})$. O'Connor and Biersack[22] suggested an improved description of the screening function $\Phi(r)$ for the Molière potential,[32] which is given by a sum of three exponential functions with $a_i = \{0.35, 0.55, 0.1\}$ and $b_i = \{0.3, 1.2, 6\}$ and the Firsov screening length[33] $a_F = 0.8854(\sqrt{Z_1} + \sqrt{Z_2})^{-2/3}$, by a correction of a_F according to the OCB screening length $a_s = a_{OCB} = [0.045(\sqrt{Z_1} + \sqrt{Z_2}) + 0.54]a_F$.

The universal ZBL and OCB potentials are smooth functions with respect to the interatomic distance r and the nuclear charge numbers Z_1 and Z_2 and, furthermore, do not take into account the individual electronic shell structure of the atoms. To consider this feature of the atomic interaction

partners it is necessary to calculate the interatomic potentials individually for each Z_1, Z_2 combination. This can be done in good approximation by assuming free electrons of density ρ in a differential volume element of the atom (statistical model of atom), where the electron density ρ is obtained from quantum-mechanical models taking into account the individual electronic properties of the atoms. In this manner, the total interaction potential can be separated into a Coulombic $V_C(r)$ and a non-Coulombic part $V_g(r)$. The first one is given by

$$V_C(r) = \frac{Z_1 Z_2}{r} + \iint \frac{\rho_1(r_1)\rho_2(r_2)}{|\vec{r} + \vec{r}_1 - \vec{r}_2|} d^3 r_1 d^3 r_2 - Z_2 \int \frac{\rho_1(r_1)}{|\vec{r} + \vec{r}_1|} d^3 r_1 - Z_1 \int \frac{\rho_2(r_2)}{|\vec{r} - \vec{r}_2|} d^3 r_2, \quad (7)$$

where $\rho_1(r_1)$ and $\rho_2(r_2)$ are the spherical electron densities of the two interacting atoms or ions and $\vec{r}_1$, $\vec{r}_2$, and $\vec{r}$ are the vectors of the distances with respect to nucleus 1, with respect to nucleus 2, and between the two nuclei, respectively. The first term on the right side in Eq. (7) describes the Coulomb repulsion between the two nuclei, the second term represents the electron-electron repulsion, and the third and fourth terms describe attractions between electrons and nuclei. The non-Coulombic part is given by

$$V_g(r) = \int E_d(\rho_1(r_1) + \rho_2(|\vec{r} + \vec{r}_1|)) d^3 r_1 - \int E_d(\rho_1(r_1)) d^3 r_1 - \int E_d(\rho_2(r_2)) d^3 r_2, \quad (8)$$

where the energy density E_d of a gas of free electrons with density ρ is a sum of the kinetic contribution given by Thomas[34] and Fermi[35] and the exchange contribution given by Bloch[36] and Dirac,[37]

$$E_d(\rho) = C_{\text{kin}} \rho^{5/3} + C_{\text{exch}} \rho^{4/3}, \quad (9)$$

with $C_{\text{kin}} = 0.3(3\pi^2)^{2/3}$ and $C_{\text{exch}} = -0.75(3/\pi)^{1/3}$ (all lengths and energies are in atomic units, a.u.). The electronic density of the two-atom system (quasimolecule) is simply approximated by a sum of the densities of the two free atoms or ions. Based on this model (with an additional small correlation contribution) and using electron densities obtained from Hartree-Fock wave functions,[38] Kim and Gordon[23,24] have calculated the interaction potentials for atomic closed-shell partners, i.e., rare gas atoms and alkali and halide ions, with their spherical densities via Gauss-Laguerre integration.

We have performed similar calculations according to Eqs. (7)−(9). However, compared with the calculations of Kim and Gordon,[23,24] we considered Roothaan-Hartree-Fock wave functions published by Clementi and Roetti[39] as described in Ref. 40. Furthermore, our calculations are not restricted to atomic closed-shell partners. In order to be able to use the analytical expression for the force $\vec{F}_{\text{string}}$ given in Eq. (6) for the classical trajectory calculations, we interpolated the Kim and Gordon and our individual HF pair potentials using the following approach:

$$V(r) = \frac{Z_1 Z_2}{r} \sum_{i=1}^{4} a_i \exp(-b_i r). \quad (10)$$

The parameters a_i and b_i $(i = 1 - 4)$ are listed in Table I.

TABLE I. Parameters a_i and b_i $(i = 1–4)$ of interpolation functions for He-, Ne-, Ar-, and N-K^+ and He-, Ne-, Ar-, and N-Cl^- individual HF potentials calculated in this work and by Kim and Gordon.[24]

	Parameter	$i = 1$	$i = 2$	$i = 3$	$i = 4$
This work					
He-K^+	a_i	−7.2835	−12.1597	6.9069	13.1362
	b_i	1.2588	1.2391	1.2044	1.2827
He-Cl^-	a_i	−7.0898	−12.8314	6.1531	14.2146
	b_i	1.1201	1.1104	1.1105	1.1201
Ne-K^+	a_i	−7.8744	−12.5389	7.4824	13.3971
	b_i	1.3291	1.3256	1.2937	1.3556
Ne-Cl^-	a_i	−7.4690	−12.7991	6.5290	14.0457
	b_i	1.1708	1.1648	1.1646	1.1710
Ar-K^+	a_i	−7.0591	−12.8746	6.3859	13.8501
	b_i	1.1506	1.1383	1.1141	1.1615
Ar-Cl^-	a_i	−7.1549	−13.0666	5.9350	14.5037
	b_i	1.0848	1.0811	1.0807	1.0853
N-K^+	a_i	−7.2708	−12.6500	6.5422	13.7998
	b_i	1.1809	1.1415	1.1159	1.1828
N-Cl^-	a_i	−7.1798	−13.0331	6.0064	14.5232
	b_i	1.0821	1.0762	1.0757	1.0826
Kim and Gordon					
He-K^+	a_i	−10.0915	−15.2996	9.7769	16.2533
	b_i	1.2397	1.2397	1.2034	1.2743
He-Cl^-	a_i	−7.3823	−12.6926	5.2158	15.2164
	b_i	0.8910	0.9709	0.8743	0.9700
Ne-K^+	a_i	−9.6213	−14.5061	9.4007	15.2314
	b_i	1.3256	1.3256	1.2942	1.3550
Ne-Cl^-	a_i	−5.5373	−13.0454	4.9075	13.9234
	b_i	0.9791	0.9914	0.9607	1.0013
Ar-K^+	a_i	−7.1565	−13.1462	6.1025	14.4595
	b_i	1.0616	1.0564	1.0289	1.0756
Ar-Cl^-	a_i	−6.1441	−13.1207	5.1898	14.2294
	b_i	0.9751	0.9957	0.9757	0.9957

In Fig. 1, we show the individual HF pair potentials calculated in this work as well as by Kim and Gordon,[24] the interpolation functions of the HF potentials, and the universal OCB and ZBL potentials for He-K, Ar-K, and N-K and He-Cl, Ar-Cl, and N-Cl. For N-K and N-Cl only the individual HF pair potentials calculated in this work are presented since the N atom is a non-closed-shell system. The Kim and Gordon potential,[23,24] however, considers the interaction for closed-shell systems as rare-gas atoms with alkali or halide ions only, so that a comparison with neutral atoms is not possible.

For all configurations, we found fair agreement between the HF potentials and the corresponding interpolation functions. In general, the HF potentials reveal a small attractive part for distances between 5 and 10 a.u. compared to the universal OCB and ZBL potentials, which are repulsive only. The HF potentials calculated by Kim and Gordon are slightly different from our HF potential for a potential energy below 0.1 eV. The ZBL potential reveals the largest repulsivity in the range of the interaction distance shown in Fig. 1. The OCB potential is weaker than the ZBL potential, but it reveals a larger repulsivity than the HF potentials. For distances below 3 a.u. or above

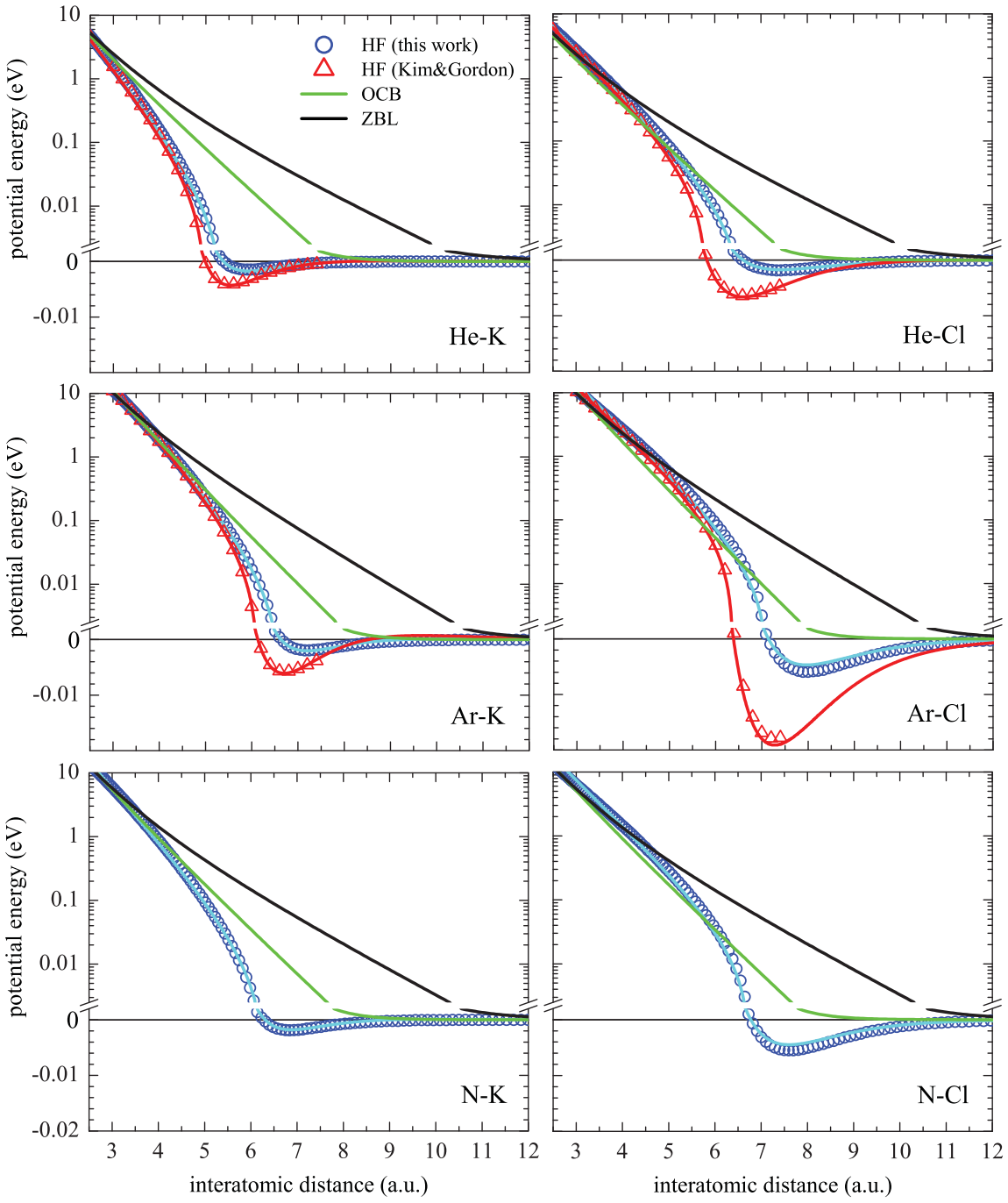

FIG. 1. (Color online) Potential energy as function of interatomic distance for (left) He-K, Ar-K, and N-K and (right) He-Cl, Ar-Cl, and N-Cl. Individual HF potentials are calculated in this work (blue circles) and by Kim and Gordon[24] (red triangles); blue and red solid curves show interpolation functions (for details, see text and Table I); green curves show OCB potential; black curves show ZBL potential. For calculation of individual HF potentials charge states of K^+ and Cl^- ions were taken into account. (Note that the upper part of the potential-energy axis is scaled logarithm, whereas the lower part is linearly scaled.)

12 a.u., where the interaction potential energy is above 10 eV or almost zero, respectively, the HF, OCB, and ZBL potentials agree.

Figure 2 shows the equipotential lines of the potential $V_{\text{surface}}(x,z)$ for scattering of He atoms along the ⟨110⟩ directions of the KCl(001) surface in an energy range 0.3−40 eV, where $V_{\text{surface}}(x,z)$ is given by a sum of He-K and He-Cl string potentials. The atomic strings along ⟨110⟩ are composed by either K^+ or Cl^- ions, whereas the atomic strings along ⟨100⟩ are composed by K^+ as well as Cl^- ions. The displayed contours were derived from HF potentials calculated in this work [Fig. 2(a)] and by Kim and Gordon[24] [Fig. 2(b)] as well as from OCB [Fig. 2(c)] and ZBL [Fig. 2(d)] potentials. For the calculation of both types of HF potentials, the charge states of

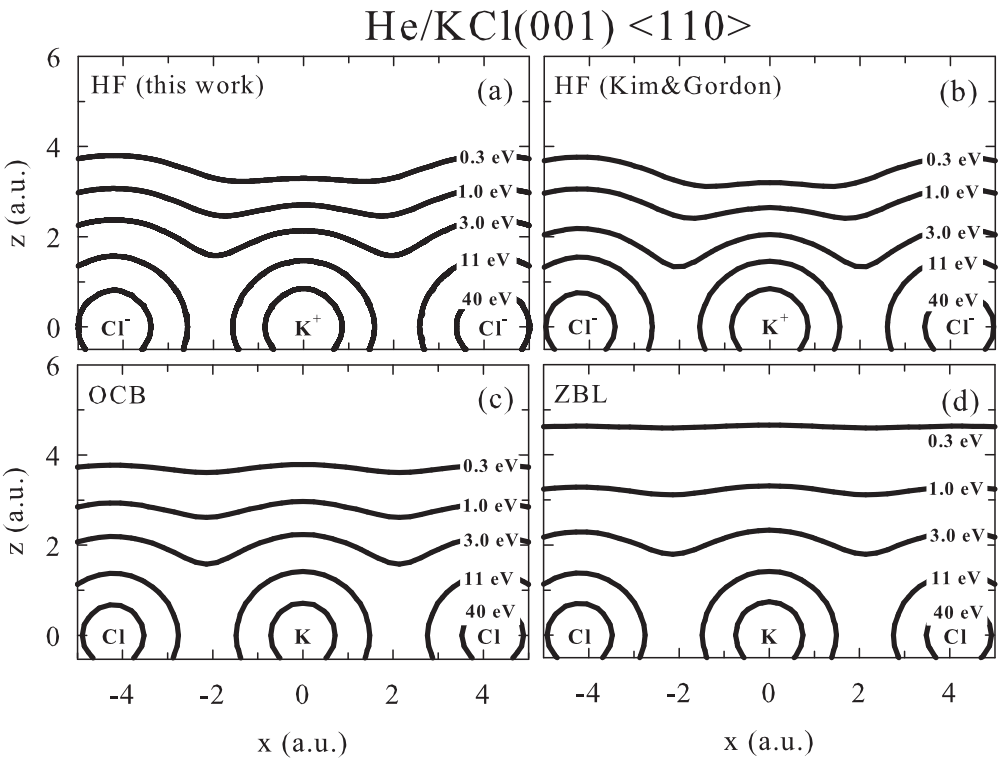

FIG. 2. Equipotential lines of potential $V_{\text{surface}}(x,z)$ for scattering of He atoms along ⟨110⟩ of KCl(001) in an energy range 0.3–40 eV, where $V_{\text{surface}}(x,z)$ is given by a sum of He-K and He-Cl string potentials. Contours are derived from individual HF potentials calculated (a) in this work, (b) by Kim and Gordon[24], and from (c) OCB and (d) ZBL potentials. For calculation of HF potentials charge states of K^+ and Cl^- ions were taken into account.

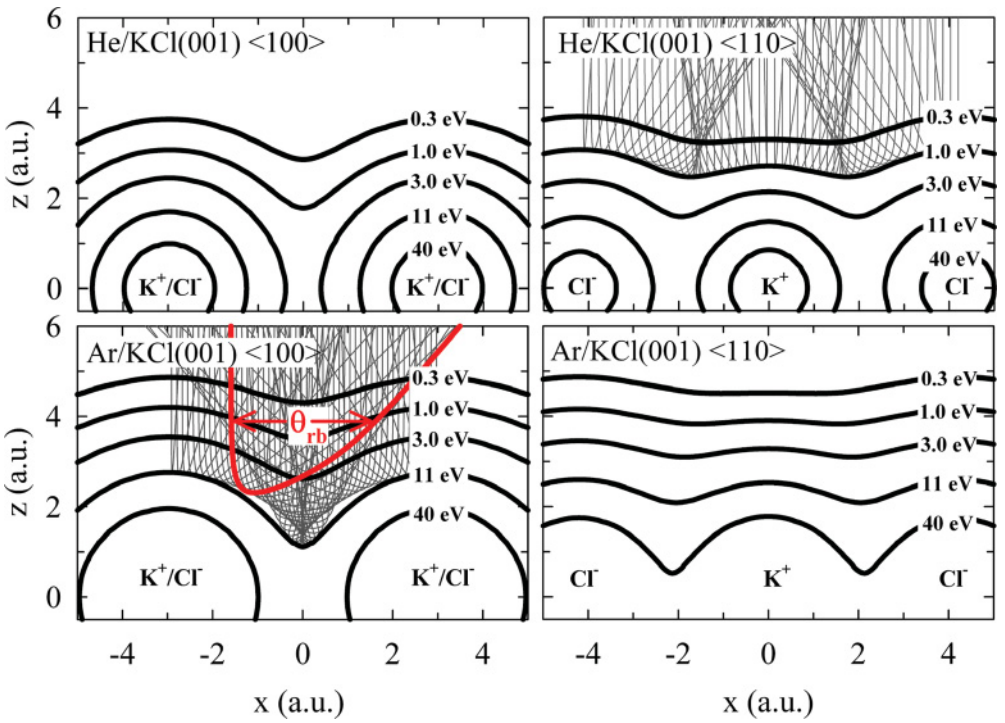

FIG. 3. (Color online) Equipotential lines of potential $V_{\text{surface}}(x,z)$ for scattering of (top) He and (bottom) Ar atoms along (left) ⟨100⟩ and (right) ⟨110⟩ of KCl(001) in an energy range 0.3–40 eV, where $V_{\text{surface}}(x,z)$ is given by a sum of He-K^+ and He-Cl^- and of Ar-K^+ and Ar-Cl^- string potentials, respectively. Contours are derived from individual HF potentials calculated in this work, where charge states of K^+ and Cl^- ions were taken into account. Projections of 50 calculated classical trajectories of He and Ar atoms with $E_\perp = 1$ eV and 11 eV scattered along ⟨110⟩ and ⟨100⟩, respectively, are shown as gray curves. Rainbow angle θ_{rb} is highlighted for scattering of Ar along ⟨100⟩.

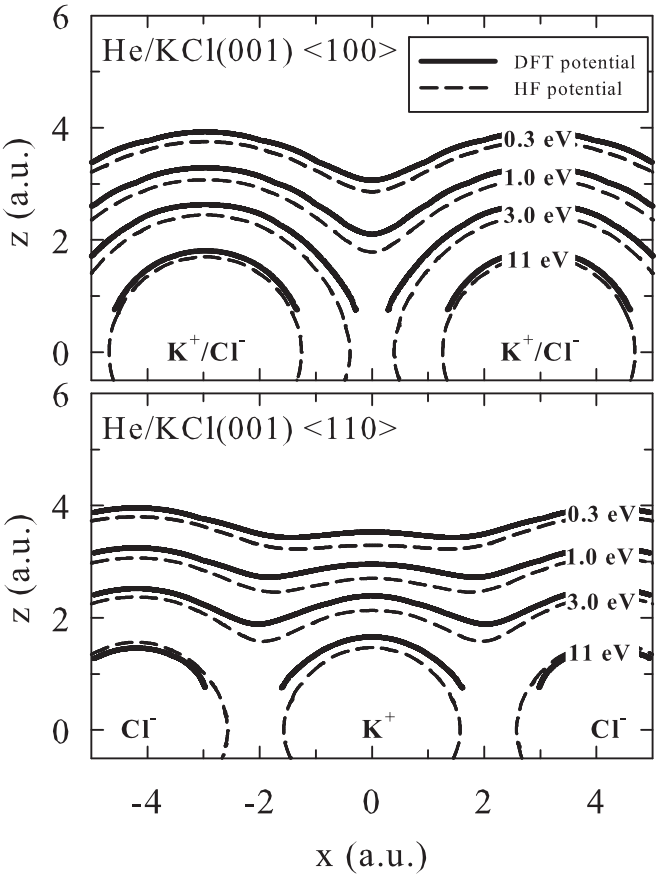

FIG. 4. Equipotential lines of potential $V_{\text{surface}}(x,z)$ for scattering of He atoms along (top) ⟨100⟩ and (bottom) ⟨110⟩ of KCl(001) in an energy range 0.3–11 eV. Contours are derived from DFT (solid curves) and individual HF (dashed curves) potentials calculated in this work, where charge states of K^+ and Cl^- ions were taken into account.

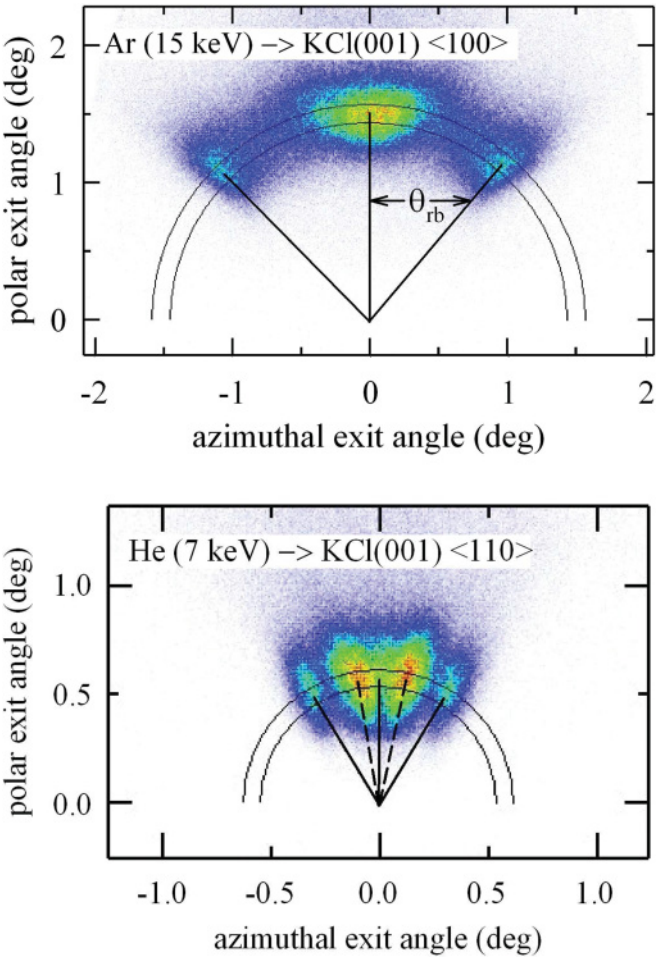

FIG. 5. (Color online) Two-dimensional plots of angular distributions recorded by means of position-sensitive microchannel plate (MCP) detector for scattering of (top) 15-keV Ar atoms along ⟨100⟩ under $\phi_{\text{in}} = 1.53°$ with $E_\perp = 10.7$ eV and (bottom) 7-keV He atoms along ⟨110⟩ under $\phi_{\text{in}} = 0.64°$ with $E_\perp = 0.9$ eV from KCl(001). Annuli mark elastic scattered projectiles; solid and dashed lines mark rainbow angles θ_{rb}. Color code for two-dimensional angular distributions is as follows: red, high intensity; blue, low intensity.

K^+ and Cl^- ions were taken into account. Due to the different repulsivities of the interatomic potentials shown in Fig. 1, the corrugations of the resulting surface potentials $V_{\text{surface}}(x,z)$ are also different. For 0.3 eV the equipotential plane of the ZBL potential is weakly corrugated, whereas the equipotential planes of the HF and OCB potentials reveal a corrugation, for example. In general, the corrugation of an interaction potential increases with increasing energy.

In Fig. 3, we show the equipotential lines of the potential $V_{\text{surface}}(x,z)$ for scattering of He (top panels) and Ar (bottom panels) atoms along the ⟨100⟩ (left panels) and ⟨110⟩ (right panels) directions of the KCl(001) surface in an energy range 0.3−40 eV, where the potential $V_{\text{surface}}(x,z)$ is given by a sum of He-K^+ and He-Cl^- and of Ar-K^+ and Ar-Cl^- string potentials, respectively. The displayed contours were derived from HF potentials calculated in this work, where the charge states of K^+ and Cl^- ions were taken into account. The projections of 50 calculated classical trajectories of He and Ar atoms with $E_\perp = 1$ eV and 11 eV scattered along ⟨110⟩ and ⟨100⟩, respectively, are shown as gray curves in Fig. 3 also. Due to the corrugation of the equipotential planes of the interaction potential, the projectiles are deflected out of the plane defined by the surface normal (z axis) and the channeling direction (y axis, here ⟨100⟩ or ⟨110⟩). The quasisinusoidal shape of the equipotential planes leads to an enhanced intensity under the maximum deflection angle, the rainbow angle θ_{rb} (highlighted in Fig. 3 for scattering of Ar atoms along ⟨100⟩ of the KCl(001) surface), which depends on the transverse energy $E_\perp$ of the projectiles and the given interaction potential only.

We also calculated DFT potentials for the scattering of He atoms from KCl(001) using the Vienna Ab-initio Simulation Package (VASP)[41,42] with the Perdew, Burke, and Ernzerhof (PBE)[43,44] exchange-correlation functional. An empirical dispersion correction was added to include the dispersion forces (PBE+D).[45–47] The electron-ion interactions were described by the projector augmented wave method (PAW), originally developed by Blöchl[48] and adapted by Kresse and Joubert.[49] The total energy calculations were performed with a plane-wave basis set with a kinetic energy cutoff of 400 eV and a $2 \times 2 \times 1$ Monkhorst-Pack k-point mesh.[50]

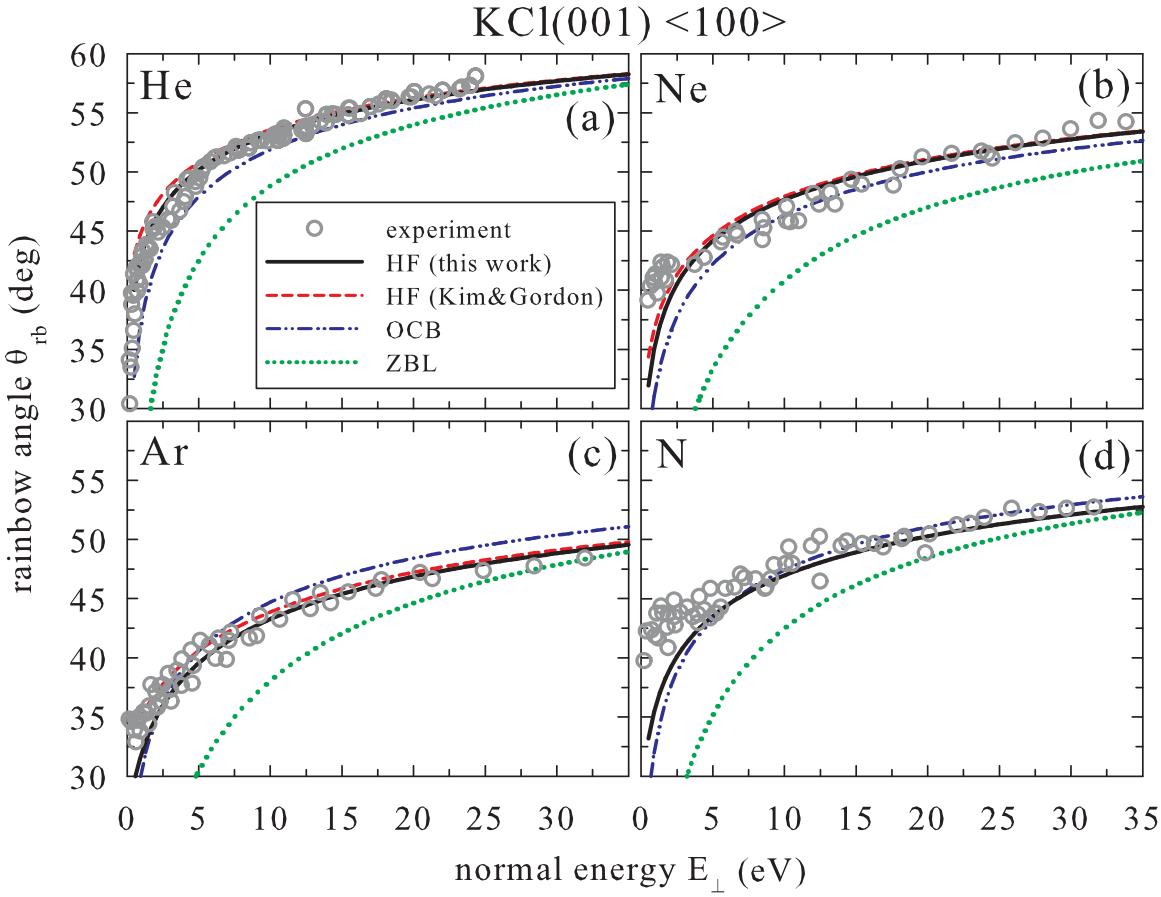

FIG. 6. (Color online) Rainbow angles θ_{rb} as function of normal energy $E_\perp$ for scattering of (a) He, (b) Ne, (c) Ar, and (d) N atoms from KCl(001) along ⟨100⟩. Gray circles represent experimental data; curves represent results from classical trajectory calculations using individual HF potentials calculated in this work (black solid curve) and by Kim and Gordon[24] (red dashed curve), OCB (blue dash-dotted curve), and ZBL (green dotted curve) potentials.

The derived contours of the equipotential lines of the potential $V_{surface}(x,z)$ derived from the DFT calculations for scattering of He atoms along the ⟨100⟩ and ⟨110⟩ directions of the KCl(001) surface are shown in Fig. 4. For comparison, the equipotential lines of the corresponding potentials obtained from the individual HF potentials calculated in this work (cf. Fig. 3) are also displayed in Fig. 4. We found very similar corrugations of the DFT and HF potentials; however, the DFT potentials are calculated for distances to the surfaces above 0.7 a.u. only due to the considered finite lattice. Hence, for the DFT potentials the rainbow angles θ_{rb} were derived from classical trajectory calculations for normal projectile energies $E_\perp$ up to 5 eV only.

B. Comparison with experimental results

In Fig. 5, we show two-dimensional plots of angular distributions recorded by means of the position-sensitive microchannel plate (MCP) detector for scattering of 15-keV Ar atoms along ⟨100⟩ under $\phi_{in} = 1.53^\circ$ with $E_\perp = 10.7$ eV (top panel) and 7-keV He atoms along ⟨110⟩ under $\phi_{in} = 0.64^\circ$ with $E_\perp = 0.9$ eV (bottom panel) from KCl(001). The annulus marks the range of elastically scattered projectiles. Both distributions show typical features for axial surface channeling, which are also visualized by the trajectories shown in Fig. 3 (note that the highlighted transverse energies in Fig. 3 are about the same as in Fig. 5). For scattering of Ar atoms along ⟨100⟩ (top panel) the angular distribution contains a pronounced central peak which stems from a double deflection of the projectiles on adjacent equivalent strings composed by K^+ as well as Cl^- ions, whereas the two different rainbow angles shown for scattering of He atoms along ⟨110⟩ (bottom panel) stem from deflections of projectiles on adjacent nonequivalent strings composed either by K^+ or Cl^- ions (cf. Fig. 3). In particular, the two separated rainbow angles were observed for scattering along ⟨110⟩ for He and Ne atoms for normal energies $E_\perp$ up to 5 eV and for Ar atoms for $E_\perp \leqslant 10$ eV, where the "inner" and "outer" rainbow angles stem from the deflection on the K^+ and Cl^- strings, respectively. The "outer" rainbow angle increases slightly for decreasing normal energy due to the attractive part of the interaction potential, which affects the trajectories of the projectiles. For enhanced normal energies, both rainbow angles increase due to the increasing corrugation of the interaction potential, and therefore, the "inner" and "outer" rainbow angles can no longer be separated.

In the same manner as demonstrated in Fig. 5, the rainbow angles θ_{rb} were determined for scattering of He, Ne, Ar, and N atoms from KCl(001) along the ⟨100⟩ and ⟨110⟩ directions for different energies E_0 and angles of incidence ϕ_{in}. The data

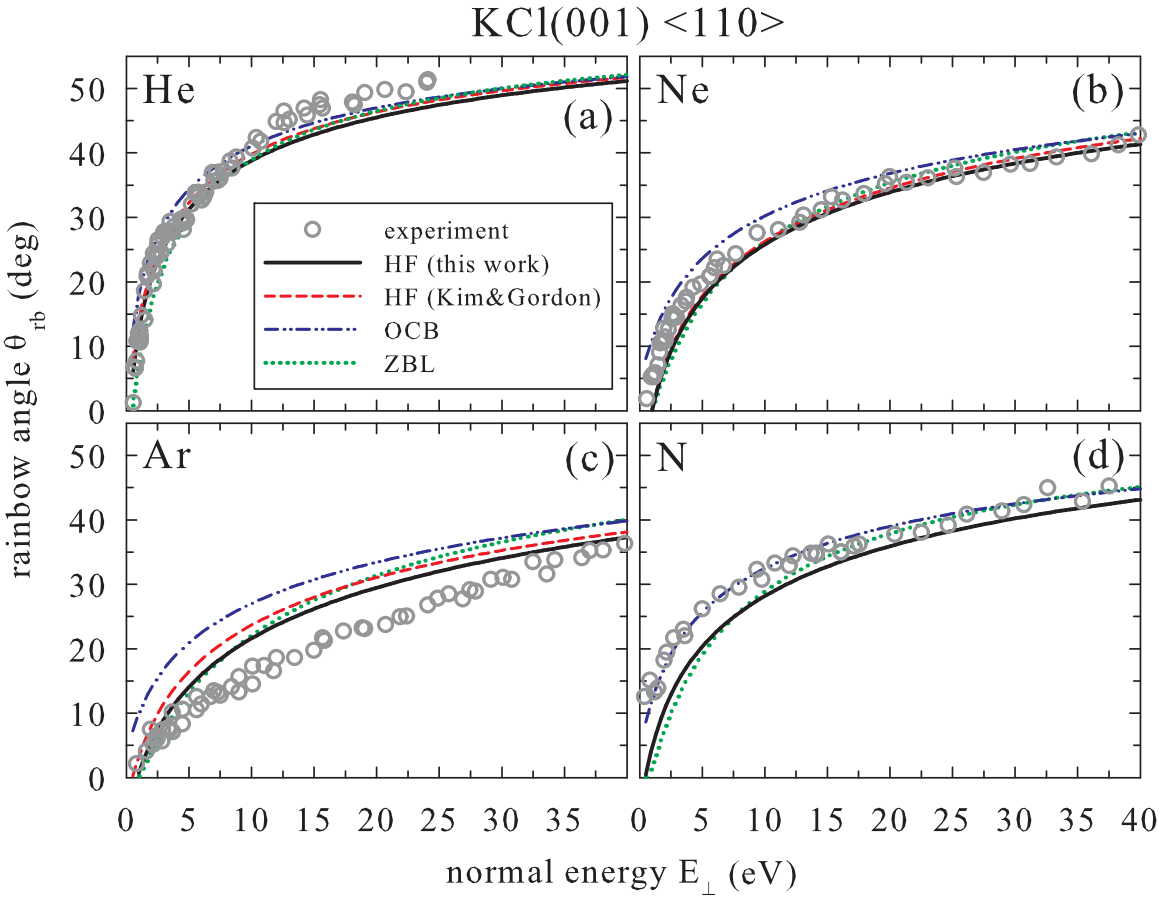

FIG. 7. (Color online) "Inner" rainbow angles θ_{rb} as function of normal energy $E_\perp$ for scattering of (a) He, (b) Ne, (c) Ar, and N atoms from KCl(001) along ⟨110⟩ (same notation as in Fig. 6).

are plotted as function of the normal energy $E_\perp = E_0 \sin^2 \phi_{in}$ in Figs. 6 and 7. For scattering along the ⟨110⟩ directions we show the "inner" rainbow angle in Fig. 7 only; however, we discuss below (at the end of this section) the normal-energy dependence of both rainbow angles by means of the data shown in Fig. 8.

Within the experimental uncertainties the results support the concept that the rainbow angle θ_{rb} is independent of the projectile energy E_0 at the same normal energy $E_\perp$. For the insulator LiF(001) we observed in recent studies for scattering of Ne, N, and O atoms no deviation from such a behavior.[19,20] However, this is different for the scattering from an aluminum surface [e.g., Al(100) or Al(111)], for example, where an additional potential due to the embedding of atomic projectiles into the electron gas at the selvedge of a metal surface affects the scattering process. Thus, for some reactive atomic projectiles, e.g., Na and Al, a dependence on the total projectile velocity was observed.[14,17] The additional contribution to the interaction potential can amount up to some eV and is repulsive for noble-gas atoms but partially attractive for reactive atoms. Local density approximation (LDA) calculations[51] support this assumption since a repulsive potential for noble-gas atoms and an attractive potential for reactive atoms forming negative ions within an electron gas were found. On a qualitative level, an additional (planar) embedding potential results in less corrugated equipotential curves for given normal energies $E_\perp$ and following smaller rainbow angles. Nevertheless, in the present study, we observed a monotonic increase of the rainbow angle θ_{rb} with increasing $E_\perp$ for all projectiles and for both channeling directions since more corrugated equipotential planes at larger potential energies result in larger rainbow angles.[14–21]

The curves shown in Figs. 6 and 7 represent results from classical trajectory calculations making use of the different types of interatomic potentials between the He, Ne, Ar, and N projectile atoms and the atoms or ions of the KCl(001) surface presented in Sec. III A. For the positions of the lattice atoms or ions an ideal structure was assumed. A small rumpling of about 0.03 Å of the topmost surface layer,[52] leading only to a small shift of the rainbow angles within the scatter of data, was neglected here. Furthermore, we neglected the rumpling since the classical rainbow angle is not suitable to deduce the rumpling value due to the uncertainty of the experimental data of about $2^\circ - 3^\circ$. However, in the regime of fast atom diffraction (FAD) with normal energies from 0.02 eV up to 1.5 eV, where quantum effects are important and affect the scattering process, one has to consider the rumpling for a comparison between experimental data and calculations.[53,54]

We found fair agreement between the experimental data and the calculated rainbow angles for both HF potentials for scattering of He, Ne, and Ar atoms along ⟨100⟩ in the whole investigated normal-energy range. Concerning the scattering of N atoms, the calculated rainbow angles considering the HF

potentials are smaller than the experimental data for normal energies $E_\perp < 5$ eV. The calculated rainbow angles for the OCB potential are slightly smaller for scattering of He, Ne, and N atoms and slightly higher for scattering of Ar atoms along ⟨100⟩ with respect to the rainbow angles calculated for both HF potentials. The calculated rainbow angles considering the ZBL potential are significantly smaller with respect to the experimental data for normal energies $E_\perp$ below 35 eV. For $E_\perp > 35$ eV, the calculated rainbow angles are in accord with the HF, the OCB, and the ZBL potentials. We note that the spread of the experimental data is slightly larger for the scattering of Ne and N atoms along ⟨100⟩. However, the quality of the experimental data is sufficient to show fair agreement between experimental and calculated rainbow angles based on HF and OCB potentials as well as the discrepancy for the ZBL potential for scattering along ⟨100⟩. This discrepancy between the experimental and calculated rainbow angles for the ZBL potential was also observed in a recent study for scattering of Ne atoms from LiF(001) along the ⟨100⟩ and ⟨110⟩ directions.[19]

Concerning the other channeling direction investigated in the present work (cf. Fig. 7), we found fair agreement between the experimental data and the calculated rainbow angles for both HF, OCB, and ZBL potentials for scattering of He atoms along ⟨110⟩ in the whole normal-energy range. For scattering of Ar atoms along ⟨110⟩, all calculated rainbow angles are larger than the experimentally deduced values for $E_\perp < 40$ eV. As a reason, we consider the completely neglected deformation of the electron densities in the projectile atoms as well as the surface in our calculations, which leads to an enhanced corrugation and a decreased repulsion of the interaction potential. In contrast to the results for scattering along ⟨100⟩, the calculated normal-energy dependence of the rainbow angle is in agreement for both HF and the ZBL potentials, whereas the values of θ_{rb} calculated using the OCB potential are slightly larger with respect to the results for the other potentials. The experimentally deduced rainbow angles for scattering of Ne and N atoms along ⟨110⟩ are between the calculated θ_{rb} for OCB and HF and the ZBL potentials.

In Fig. 8, we show the experimental rainbow angles θ_{rb} as a function of the normal energy $E_\perp$ in a range from 0.1 eV up to 4.8 eV for scattering of He atoms from KCl(001) along ⟨100⟩ (top panel) and ⟨110⟩ (bottom panel). With respect to the data shown in Fig. 7, we plotted in the bottom panel of Fig. 8 the "inner" and "outer" rainbow angles. The curves represent results from classical trajectory calculations using the DFT and HF potentials calculated in this work. For scattering along ⟨100⟩, we found good agreement between the experimental data and the calculations using the DFT and HF potentials for normal energies $0.5 \text{ eV} \leqslant E_\perp \leqslant 5$ eV. For scattering of He atoms along ⟨110⟩, the calculated values of the "inner" rainbow angle using the HF potential are in agreement with the experimental data, and the values of θ_{rb} calculated using the DFT potential are slightly smaller by about 2° with respect to the experimental data. However, the calculated values of the "outer" rainbow angle are too large with respect to the experimental data for the DFT and HF potentials, where we found poor agreement for the HF potential.

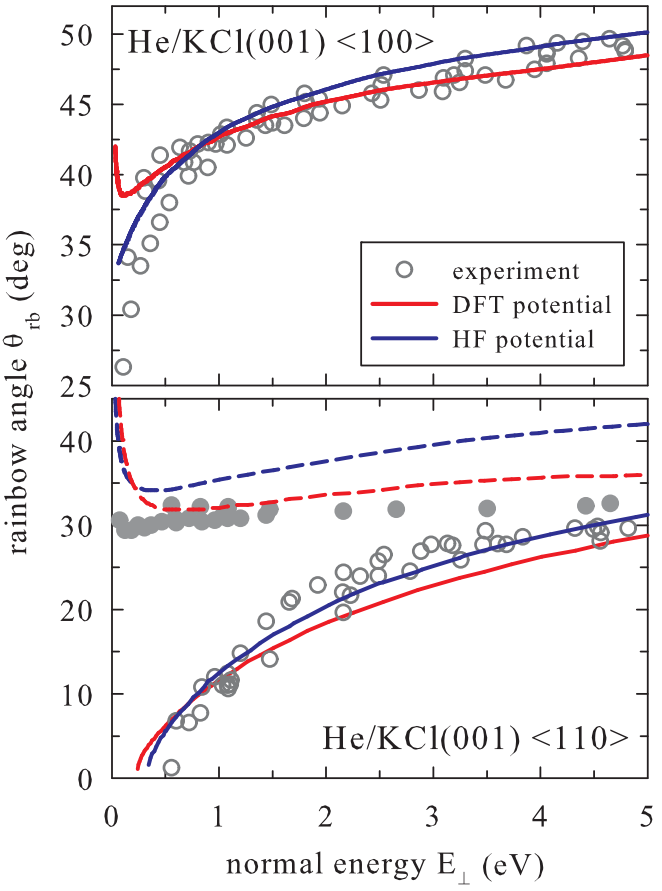

FIG. 8. (Color online) Rainbow angles θ_{rb} as function of normal energy $E_\perp$ in a range 0.1–4.8 eV for scattering of He atoms from KCl(001) along (top) ⟨100⟩ and (bottom) ⟨110⟩ as shown in Figs. 6 and 7. Open gray circles represent experimental data, and the solid gray circles in the bottom panel represent experimentally determined values of the "outer" rainbow angle (not shown in Fig. 7; for details see text). Curves represent results from classical trajectory calculations using DFT potential (red solid and dashed curves) and individual HF potential (blue solid and dashed curves).

IV. CONCLUSIONS

In conclusion, we have presented an analysis of rainbow structures observed for the scattering of He, Ne, Ar, and N atoms from KCl(001) along the ⟨100⟩ and ⟨110⟩ axial channeling directions in the surface plane. The well-defined peaks in the angular distributions of scattered atoms allow us to analyze the experimental data in terms of the effective interaction potentials by comparing with classical trajectory calculations based on different potentials. It turns out that the rainbow angles are closely related to the corrugation of the equipotential planes. This feature is the basis for detailed tests on established approaches for atomic interaction potentials in an interval of distances to the surface from about 1 to 5 a.u. For the specific case studied in the present work, we found an overall good description of the experimental data by the individual Hartree-Fock (HF) pair potentials calculated by Kim and Gordon as well as within the present study, whereas potentials with the ZBL screening function are generally too repulsive for larger distances. Accordingly, we found for the

ZBL potential poor agreement between the experimental data and the results of the calculation for the scattering along ⟨100⟩ only; however, for scattering along the ⟨110⟩ directions the agreement is good. We also reveal that the application of a correction of the screening length in the Molière potential as proposed by O'Connor and Biersack results in a better agreement with the experimental data as for the ZBL potential. Comparing the DFT and the HF potential for the scattering of He atoms from KCl(001), we found no significant differences in the description of the experimental data for these completely different derived potentials.

ACKNOWLEDGMENTS

The authors thank K. Maass and G. Lindenberg for their assistance in the preparation and running of the experiments. This work was supported by the Deutsche Forschungsgemeinschaft under Contracts No. Wi 1336 and Sfb 546.

*Corresponding author: mbusch@physik.hu-berlin.de

[1] E. W. McDaniel, J. B. A. Mitchell, and M. E. Rudd, *Atomic Collisions* (Wiley, New York, 1993).
[2] N. F. Mott and H. S. W. Massey, *The Theory of Atomic Collisions* (Oxford University Press, Oxford, 1965).
[3] J. F. Ziegler, J. P. Biersack, and U. Littmark, *The Stopping and Range of Ions in Solids* (Pergamon Press, New York, 1985), Vol. 1.
[4] H. Niehus, E. Taglauer, and W. Heiland, Surf. Sci. Rep. **17**, 213 (1993).
[5] H. Niehus, *Practical Surface Analysis* (Wiley, Chichester, 1992), Vol. 2.
[6] J. F. van der Veen, Surf. Sci. Rep. **5**, 199 (1985).
[7] E. S. Mashkova and V. A. Molchanov, *Medium-Energy Ion Reflection from Solids*, Modern Problems in Condensed Matter Sciences Vol. 11 (North-Holland, Amsterdam, 1986).
[8] H. Winter, Phys. Rep. **367**, 387 (2002).
[9] J. D. McClure, J. Chem. Phys. **51**, 1687 (1969).
[10] J. D. McClure, J. Chem. Phys. **52**, 2712 (1970).
[11] F. O. Goodman, Surf. Sci. **26**, 327 (1971).
[12] R. Sizmann and C. Varelas, Nucl. Instrum. Methods **132**, 633 (1976).
[13] A. W. Kleyn and T. C. M. Horn, Phys. Rep. **199**, 191 (1991).
[14] A. Schüller, G. Adamov, S. Wethekam, K. Maass, A. Mertens, and H. Winter, Phys. Rev. A **69**, 050901(R) (2004).
[15] A. Schüller, S. Wethekam, A. Mertens, K. Maass, H. Winter, and K. Gärtner, Nucl. Instrum. Methods Phys. Res. Sect. B **230**, 172 (2005).
[16] H. Winter and A. Schüller, Nucl. Instrum. Methods Phys. Res. Sect. B **232**, 165 (2005).
[17] A. Schüller and H. Winter, Nucl. Instrum. Methods Phys. Res. Sect. B **256**, 122 (2007).
[18] A. Schüller and H. Winter, Nucl. Instrum. Methods Phys. Res. Sect. B **261**, 578 (2007).
[19] A. Schüller, H. Winter, and K. Gärtner, Europhys. Lett. **81**, 37007 (2008).
[20] A. Schüller and H. Winter, Nucl. Instrum. Methods Phys. Res. Sect. B **267**, 2621 (2009).
[21] P. Tiwald, A. Schüller, H. Winter, K. Tökesi, F. Aigner, S. Gräfe, C. Lemell, and J. Burgdörfer, Phys. Rev. B **82**, 125453 (2010).
[22] D. J. O'Connor and J. P. Biersack, Nucl. Instrum. Methods Phys. Res. Sect. B **15**, 14 (1986).
[23] R. G. Gordon and Y. S. Kim, J. Chem. Phys. **56**, 3122 (1972).
[24] Y. S. Kim and R. G. Gordon, J. Chem. Phys. **60**, 4323 (1974).
[25] J. Lindhard, Mat. Fys. Medd. Dan. Vid. Selsk. **34**, 1 (1965).
[26] B. R. Appleton, C. Erginsoy, and W. M. Gibson, Phys. Rev. **161**, 330 (1967).
[27] D. S. Gemmell, Rev. Mod. Phys. **46**, 129 (1974).
[28] Q. K. K. Liu, J. P. Biersack, and M. Posselt, Nucl. Instrum. Methods Phys. Res. Sect. B **102**, 3 (1995).
[29] C. Erginsoy, Phys. Rev. Lett. **15**, 360 (1965).
[30] J. Burgdörfer and C. Lemell, in *Slow Heavy-Particle Induced Electron Emission from Solid Surfaces*, Springer Tracts in Modern Physics Vol. 225 (Springer, Berlin, 2007), p. 1.
[31] H. M. Macdonald, Proc. London Math. Soc. **30**, 165 (1898).
[32] G. Molière, Z. Naturforsch. A **2**, 133 (1947).
[33] O. Firsov, Zh. Eksp. Teor. Fiz. **33**, 696 (1957).
[34] L. H. Thomas, Proc. Cambridge Philos. Soc. **23**, 542 (1927).
[35] E. Fermi, Z. Phys. **48**, 73 (1928).
[36] F. Bloch, Z. Phys. **57**, 545 (1929).
[37] P. A. M. Dirac, Proc. Cambridge Philos. Soc. **26**, 376 (1930).
[38] E. Clementi, IBM J. Res. Dev. Suppl. **9**, 2 (1965).
[39] E. Clementi and C. Roetti, At. Data Nucl. Data Tables **14**, 177 (1974).
[40] K. Gärtner and K. Hehl, Phys. Status Solidi B **94**, 231 (1979).
[41] G. Kresse and J. Furthmüller, Comput. Mater. Sci. **6**, 15 (1996).
[42] G. Kresse and J. Furthmüller, Phys. Rev. B **54**, 11169 (1996).
[43] J. P. Perdew, K. Burke, and M. Ernzerhof, Phys. Rev. Lett. **77**, 3865 (1996).
[44] J. P. Perdew, K. Burke, and M. Ernzerhof, Phys. Rev. Lett. **78**, 1396 (1997).
[45] S. Grimme, J. Comput. Chem. **25**, 1463 (2004).
[46] S. Grimme, J. Comput. Chem. **27**, 1787 (2006).
[47] T. Kerber, M. Sierka, and J. Sauer, J. Comput. Chem. **29**, 2088 (2008).
[48] P. E. Blöchl, Phys. Rev. B **50**, 17953 (1994).
[49] G. Kresse and D. Joubert, Phys. Rev. B **59**, 1758 (1999).
[50] H. J. Monkhorst and J. D. Pack, Phys. Rev. B **13**, 5188 (1976).
[51] M. J. Puska and R. M. Nieminen, Phys. Rev. B **43**, 12221 (1991).
[52] J. Vogt and H. Weiss, Surf. Sci. **491**, 155 (2001).
[53] U. Specht, M. Busch, J. Seifert, H. Winter, K. Gärtner, R. Włodarczyk, M. Sierka, and J. Sauer, Nucl. Instrum. Methods Phys. Res. Sect. B **269**, 799 (2011).
[54] A. Schüller, D. Blauth, J. Seifert, M. Busch, H. Winter, K. Gärtner, R. Włodarczyk, J. Sauer, and M. Sierka, Surf. Sci. (2011), in press.